Indian Journal of Pure & Applied Physics
Vol. 62, February 2024, pp. 133-143
DOI: 10.56042/ijpap.v62i2.7694

Dielectric Properties of Dual Phase (Cu-Zn-Ni-Mg-Fe)O High Entropy Oxide

Anshu K Jha, Amit K Gupta, Priyanka Kumari & Rohit R Shahi*

Functional Material Research Laboratory, Department of Physics, Central University of South Bihar Gaya 824 236, India

Received 31 December 2023; accepted 25 January 2024

A mixture of spinel and rock-salt phase was synthesized for (Cu-Zn-Ni-Mg-Fe)O HEO High Entropy Oxide (HEO) through the modified solid-state synthesis and studied for the dielectric properties. Three different (Cu-Zn-Ni-Mg-Fe)O HEO samples were synthesized by the variation of synthesis parameters, *i.e*., 10 hour (hr) ball-milling followed by sintering at 1050 °C for 20 hr (10BM-HEO-20), 20 hr ball-milling followed by sintering at 1050 °C for 20 hr (20BM-HEO-20) and sintering for 10 hr (20BM-HEO-10) separately. The synthesized samples were studied for the effect of synthesis parameters on phase evolution and their correlation with dielectric properties. The volume phase fraction for the spinel and rock-salt phase changed with the variation of the synthesis parameters**.** The value of dielectric constant decreased for the sample 10 BM-HEO-20, 20BM-HEO-20 and 20 BM-HEO-10 HEOs due to the synergistic effect of decrease in particle size, volume phase fraction of spinel phase as well as more distorted unit cells of spinel HEO phase. The value of dielectric loss is in decreasing trend for 10BM-HEO-20, 20BM-HEO-20 and 20BM-HEO-10 samples. The value of the dispersion factor for 10BM-HEO-20, 20BM-HEO-20, and 20BM-HEO-10 are found to be 1.839, 2.313, and 2.156, respectively. The present study provides insight the dielectric properties of HEO can be tuned broadly by the change in the synthesis parameters.

Keywords: High entropy oxide; Solid state synthesis; dielectric properties; Ball-milling

1 Introduction

In 2004, a new method for alloy design was introduced independently by Cantor *et al.* and Yeh *et al.*[1,2]. They simultaneously developed different single-phase multi-principal alloys with more than five alloying elements in an equimolar ratio[1,2]. Through this approach new class of materials named High Entropy Alloy (HEA) bring forth in the material world, exhibiting unique, extraordinary tuneable, and multifunctional properties[3]. HEAs have many-fold benefits over conventional alloys. Furthermore, different High Entropy Materials (HEMs) such as high entropy oxides, high entropy metal borides, high entropy nitrides, high entropy carbides, and high entropy sulphides were synthesized and reported as a potential material for different functional properties[4-10].

Based on the concept of HEA, Rost *et al.* synthesized rock-salt phase structure of $(Mg_{0.2}Co_{0.2}Cu_{0.2}Ni_{0.2}Zn_{0.2})O$ HEO with equimolar ratio of constituent oxides (MgO, CoO, CuO, NiO, ZnO) and concluded that mixed HEO phase was formed at low temperatures due to the dominance of the enthalpy effect over entropy[4]. However, single rock-salt phase was formed at high-temperature because the configurational entropy effect was more pronounced than enthalpy at high temperatures[4].Till now, different HEOs have been developed by the variation of constituent oxides and/or by the change in the composition of particular constituent elements[11-14]. These HEOs have different phase structures and microstructures, which possess unique tuneable functional properties. Several HEOs have also been synthesized with different crystal structures such as spinel, fluorite, perovskite, rock-salt, bixbyite, magneto plumbite, pyrochlore, and O3-type layered[4,15-25]. HEOs have extraordinary potential to overcome the limitations of conventional oxide materials due to the presence of different cations in a single lattice, which creates a synergistic effect on the overall properties of a particular HEO[26]. Recent reports confirmed that HEO has extraordinary structural-compositional property correlation and can be considered vital technological materials for different applications such as electrochemical, catalytic, magnetic, and as an electrode for battery and supercapacitors[13,27-38].

Recent reports confirmed that HEOsalso possessed excellent tuneable dielectric performance[39-41]. The multiple transition metal cations or rare earth cations in the oxygen sublattice creates a unique synergetic effect on the dielectric properties of HEO. Moreover,

*Corresponding author:
(E-mail: rohitrshahi@cusb.ac.in; rohitrshahi@gmail.com)

the dielectric properties of HEO can be significantly tuned with other functional properties either by variation of different cations or by the variation of composition of a particular cation in the HEO. Rodor *et al*. synthesized a novel (ZnMgNiFeCd)Fe_2O_4 high entropy ferrite structure[42]. They discussed that the polarization occurred due to the mobility of electrons between Fe(+2) and Fe (+3) ions in the ferrite structure[42]. Also, they concluded that the reason behind the A.C. conductivity is the transfer of charge carriers between Fe^{+2} and Fe^{+3} ions through quantum mechanical tunneling. The dispersion in permittivity and modulus was driven by the charge carriers' short and long-range mobility[42]. In another study, Ba ($Zr_{0.2}Ti_{0.2}Sn_{0.2}Hf_{0.2}Me_{0.2}$) O_3 perovskite structured HEO was synthesized by the solid-state synthesis method[43].This study also confirmed the role of high configurational entropy on phase formation through the selection of different transition metal cations in place of Me = Y^{3+}, Nb^{5+}, Ta^{5+}, V^{5+},Mo^{6+}, W^{6+}[43]. They found excellent temperature stability of permittivity in the temperature range of 25 to 200 °C, and low dielectric loss (0.002) occurred in the frequency range of 20Hz to 2MHz. It has been concluded that tuneable perovskite structure can be synthesized by the variation of configurational entropy. Vinnik *et al.* developed a single-phase perovskite structure of ($Na_{0.30}$ $K_{0.07}Ca_{0.24}La_{0.18}Ce_{0.21}$)$TiO_3$ HEO through solid state method and compared the dielectric properties of ($Na_{0.30}$ $K_{0.07}Ca_{0.24}La_{0.18}Ce_{0.21}$) TiO_3HEO and $BaTiO_3$ system[44]. They reported that the dielectric permittivity of the HEO system increased quickly at lower temperatures (200-300 °C) as compared with the $BaTiO_3$ (~400 °C) system specifically for the low-frequency range. The tangent loss for the developed HEO system was found to be higher as compared to $BaTiO_3$ at different frequency[44].

Stygar *et al*. synthesized seven different equimolar compositions of Co-Cr-Fe-Mg-Mn-Ni-O HEO[45]. The HEO system was synthesized through solid-state method at sintering temperature range of 900-1100 °C. They found that (Co-Cr-Fe-Mg-Mn-Ni-O), (Co-Cr-Fe-Mg-Ni-O), (Co-Cr-Mg-Mn-Ni-O) and (Co-Fe-Mg-Mn-Ni-O HEO exhibited dual phase *i.e.* rocksalt and spinel structure at sintered temperature of 1000 °C. However, in the case of (Co-Cr-Fe-Mg-Mn-O), (Co-Cr-Fe-Mn-Ni-O), and (Cr-Fe-Mg-Mn-Ni-O) only spinel phase structure was formed.

Although only few reports are available on the dielectric properties of HEO, the reported studies showed promising and tuneable dielectric behaviour of these materials. Here, we synthesized novel(Cu-Zn-Ni-Mg-Fe)OHEO by a modified solid-state synthesis and investigated the effect of synthesis parameters (ball-milling duration and sintering duration) on phase evolution and dielectric properties. Three different samples were synthesized through different ball-milling durations followed by the sintering at 1050 °C for different durations, *i.e*., 10 hr and 20hr, and investigate in detail about the phase formation microstructure and their correlation with the dielectric properties of the synthesized (Cu-Zn-Ni-Mg-Fe)OHEO samples.

2 Materials and Method

A modified solid-state synthesis method was adopted to synthesize novel (Cu-Zn-Ni-Mg-Fe)O HEO. The initial constituent oxides, *i.e*., CuO, MgO, NiO, ZnO, and $Fe2O_3$, whose particle size ranges from 50 to 100 μm, were taken in equimolar ratio to synthesize the HEOs. Three different synthesis approaches were adopted to synthesize (Cu-Zn-Ni-Mg-Fe)O HEO. Initially, the constituent oxides are admixed through a motorized mixer and sintered at 1050 °C for 20hr. Secondly, the mixture of initial constituent oxides is pre-milled for 10hr and sintered at 1050 °C for 10hr and 20hr, separately. Further, to investigate the effect of pre-ball-milling duration on the phase formation, the constituent oxides are pre ball-milled for 20hr, then sintering at 1050 °C for 10hr and 20hr. The planetary ball-miller was used to reduce the particle size of the constituent oxides and also get a homogeneous distribution of the selected constituent oxides for proper diffusion. The ball-milling of initial constituents oxides was performed in a hardened steel vail with zirconia balls for a different duration. The milling was performed in the indigenously developed Ball Miller in the vail of volume 250 ml at 400 RPM with the ball-to-powder weight ratio of 25:1. All the ball-milled samples were pelletized by a hydraulic press machine with 10-ton load. The pelletized samples were sintered at 1050 °C for different duration in a preheated furnace followed by room temperature cooling.

The structural analysis of the synthesized samples was performed through the XRD (Rigaku-smart lab S.E.) with the wavelength of Cu Kα = 0.15406 nm at an operating voltage of 40 kV, with a current of 40 mA. The XRD data were recorded with a step size of 0.02 and scan speed of 5° per minute for 2θ range

10° to 100°. The XRD analysis of the samples was performed through JANA-2006 software. The crystallite size and lattice strain of different synthesized HEOs samples were evaluated through the pseudo-voigt function analysis[46]. The microstructure analysis of HEO samples was studied through a Field Emission Scanning Electron Microscope (FE-SEM) at 10 kV accelerating voltage (JEOL-JSM-6380A). The PSM-1735 Numertriq frequency response analyzer was used to performed dielectric measurements. The dielectric parameters of different samples were observed through the frequency analyzer in the frequency range of 10^3-10^6Hz and in the temperature range of 25 °C -200 °C. Silver paste has coated on both sides of the sample before the measurement process. The thickness and area of 10BM-HEO-20, 20BM-HEO-20, and 20BM-HEO-10 samples used for the dielectric measurements are 1.02 & 11.09, 1.02 &66.15, 1.28 mm & 63.5 mm^2 respectively.

3 Results and Discussion

Initially, the constituent oxides were admixed and sintered at 1050 °C for 20hr.The supplementary Fig. S1(a), represents the XRD pattern of admixed constituent oxides. All the peaks are indexed with the peaks of the constituent oxides. Fig. S1(b)represents the XRD pattern of the sintered sample at temperature 1050 °C for 20hr, reveals the formation of the mixture of spinel and rock-salt phase structure with low-intensity peaks at 2θ position 34.32°, 35.57°, 36.21°, 42.69°, 56.67°, 62.34° which are identified as the un-diffused initial constituent oxides. Thus, it can be concluded that the admixing is not sufficient to get the homogeneous distribution of particles of five different constituent oxides for proper diffusion and hence, the formation of pure HEO phase does not occur through this synthesis approach. The peaks marks with arrow in Fig. S1(b), represent the peaks of undiffused oxides.

In order to enhance the diffusion of constituent oxides for the synthesis of HEO phase. In the second synthesis approach, the mixture of constituent oxides was initially ball-milled for 10 hr followed by sintering at 1050 °C for 10hr and 20hr, separately. Fig. 1(a) represents the XRD pattern of a 10 hr ball-milled mixture of constituent oxides and it reveals the presence of peaks corresponding to the initially selected oxides. Considerable broadening can be seen in the ball-milled sample due to the incorporation of significant lattice strain and reduction of the crystallite size of the constituent oxides. Fig. 1(b) represents the XRD pattern of a pre-milled sample sintered at 1050 °C for 10hr. The XRD analysis reveals the formation of a mixture of spinel and rock-salt phase indexed with space groupFd-3m and Fm-3m, respectively (fitted through Jana 2006 software). Some low intensities peaks can also be seen at 2θ= 36.46°. This may correspond to the initial constituent ZnO. For the synthesis of complete HEO phase, the ball-milled sample was further sintered at 1050 °C for 20 hr. From the XRD pattern (shown in Fig. 1(c)), it can be seen that the sample sintered at 1050 °C for 20hr has only peaks corresponding to the spinel and rock-salt phase structure of the HEO phase. The XRD pattern is further analyzed in detail through

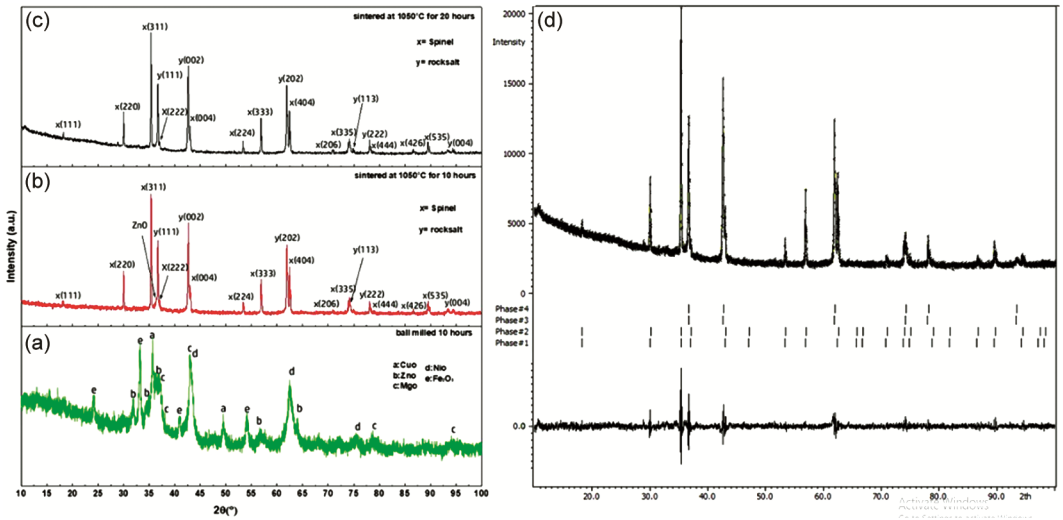

Fig. 1 — XRD patterns of (a) 10 hr ball-milled constituent oxide, (b) sample sintered at 1050 °C for 10 hr, (c) sample sintered at 1050 °C for 20 hr, (d) The Le-bail fitting of 10BM-HEO-20.

the Le-bail refinement of XRD data by Jana 2006 software. All the observed peaks are indexed with Bragg's position obtained by considering space group Fd-3m and Fm-3m for spinel and rock-salt structure, respectively. Thus, the formation of the HEO phase is confirmed by the refinement of XRD data and the sample is abbreviated as 10BM-HEO-20. The lattice parameter for the formed spinel and rock-salt phases are 8.4083Å and 4.2388Å, respectively, determined through the best-fitted XRD data. The phase fraction of spinel to rock-salt phase is estimated through the intensity ratio of most intense spinel ($I_{(311)}$), and rock-salt ($I_{(002)}$) peak is evaluated and found to be 1.38. The relative volume phase fraction of the synthesized sample was also evaluated through the following formula Eq. [46]1.

$$\text{Phase fraction } (R_T) = \frac{T}{\sum Ti} * 100\% \quad ...(1)$$

In equation (1), $R_{T.}$ expresses the volume fraction of the phase, T represents the relative intensity, and $\sum Ti$ the summation of the relative intensity of all phases indexed in the XRD pattern. For 10BM-HEO 20 sample, the respective volume phase fraction for spinel and rock-salt phase was found to be 58 and 42 %, respectively.

Further to investigate the effect of pre-ball-milling duration on the phase formation, the constituent oxides are initially prolonged ball-milled for 20hr and then sintered at 1050 °C for 10hr and 20hr, separately. Fig. 2(a) represents the XRD pattern of 20hr ball-milled initial constituent oxides and reveals the significant broadening in the most intense peak of the constituent oxides as well as low intense peaks of these oxides are now disappeared due to the reduction in the crystallite size and crystallinity after prolong milling. Fig. 2(b) represents the XRD pattern of the 20hr ball-milled sample followed by sintering at 1050 °C for 20hr. The Le-Bail fitting of the XRD pattern confirms that the mixture of spinel and rock-salt phases are formed for this synthesis approach. This sample is abbreviated as 20BM-HEO-20.The 20hr ball-milled sample is also separately sintered at 1050 °C for 10 hr. Fig. 2(c) represented the XRD pattern of sample ball-milled for 20hr and sintered at 1050°C for 10hr. As can be seen from the XRD pattern, all the peaks are indexed to the spinel and rock-salt phase structure. This sample is abbreviated as 20BM-HEO-10. Fig. 2(d,e) represent the Le-bail fitting of 20BM-HEO-20and 20BM-HEO-10 samples, respectively. The intensity ratio of the most intense peak of spinel (I_{311}) and rock-salt (I_{002}) of (Cu-Zn-Ni-Mg-Fe)O HEO is found to be 1.17 and 1.07 for 20BM-HEO-20 and 20BM-HEO-10 samples, respectively. This clearly indicates that for same duration pre-milled (20 hr BM) sample, the volume phase fraction of rock-salt phase is increased with decreasing sintering duration. The respective volume phase fraction of rock-salt HEO phase and spinel HEO phases are 46% & 54% and 49 %, & 51 % for

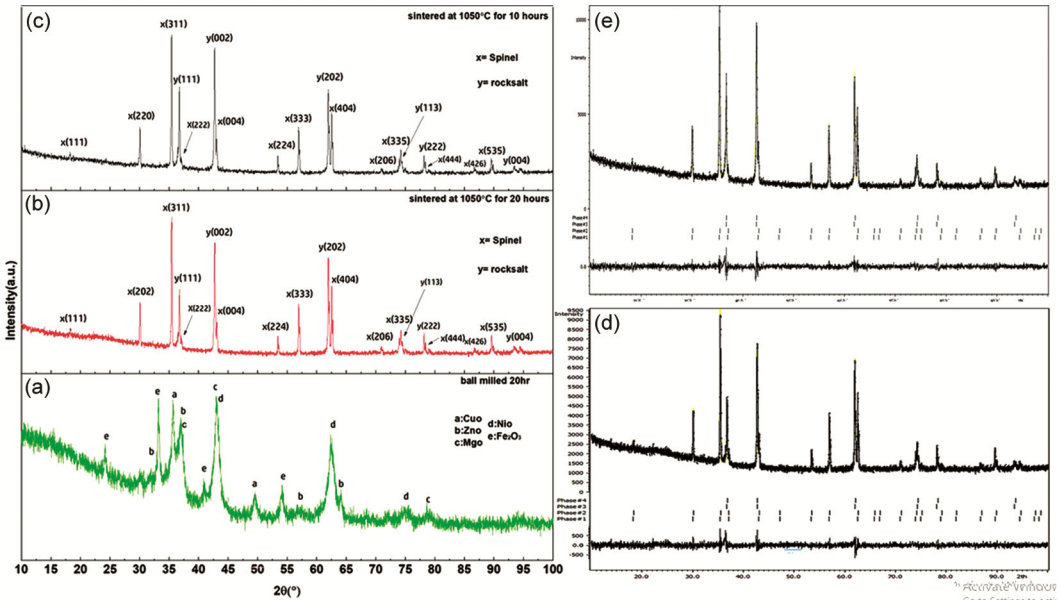

Fig 2 — Represent the XRD patterns of (a) mixture of constituent oxide ball-milled for 20 hr, (b) XRD pattern of 20BM-HEO-20, (c) XRD pattern of 20BM-HEO-10 sample, (d) and (e) are the Le-bail refinement of 20BM-HEO-20 and 20BM-HEO-10 samples, respectively.

20BM-HEO-20 and 20BM-HEO-10 samples, respectively.

Table 1 summarizes the different structural parameters evaluated through the detailed XRD analysis. The crystallite size for both the synthesized phases increases and strain decreases with an increase in sintering duration. Moreover, a significant change can be observed in the ratio of $I_{(311)S}/I_{(002)R}$ peaks. From the detailed XRD analysis of different synthesized samples, we can conclude that the mixture of pure HEO phase (spinel and rock-salt HEO phase) is formed with increasing pre-milling duration. Pre-milling before the sintering provides two-fold benefits: first, it homogenizes the particle distribution of constituent oxides (regarding size), and second, it incorporates lattice strain of the constituent oxide. Both these effects provide a driving force for the homogenous proper diffusion of constituent oxides and hence only the formation of HEO phases are occurred. Even we found that 10hr sintering is sufficient to synthesize a mixture of pure spinel and rock-salt HEO phase structure for 20 hr pre-milled samples. The mixture rock-salt and spinel phase was occurred because we selected both divalent and trivalent initial constituent oxides for the synthesis of HEO samples.

Figure 3 represents the SEM micrographs of HEO samples synthesized at different synthesis parameters. The microstructure analysis confirms the formation of faceted particles of various sizes for all the HEO samples as shown in Fig 3(a-c). The average agglomerated particle size of small and large particles of 10BM-HEO-20, 20BM-HEO-20, and 20BM-HEO-10 are found to be 0.388 & 27.46 μm, 0.414 & 34.47 μm and 0.469 & 75.92 μm, respectively. However, the average grain size for 10BM-HEO-20, 20BM-HEO-20, and 20BM-HEO-10samples are found to be 6, 52, 8.25 and 10.9 μm respectively. It has been found that the 20BM-HEO-10 sample has large particles as compared to the other two synthesized samples. As can be seen from 3(c) 20BM-HEO-10 sample has also large numbers of pores whose size ranges from 6.54 μm and 12.95μm. These pores may form because in sintering process there are agglomeration phenomenon inside the constituent oxides and the arrangement of atoms at grain boundaries are irregular with low atomic density, and grain growth is faster than the diffusion of the grain these phenomenon resulting the formation of holes at the grain boundaries. The elemental analysis for the samples having HEO phase was performed through the elemental mapping and shown in Fig. 4. From the figure, it can be seen that the cation of Cu, Mg, Ni, Zn, and Fe have homogenously dispersed throughout the region for 10BM-HEO-20, 20BM-HEO-20, 20BM-HEO-10 samples. EDAX spectra is also recorded from random three-four region and found that for each selected place all the cations are present in the equimolar ratio.

Dielectric properties of different HEO samples synthesized at different synthesis parameters are investigated in detail. These investigations include the dielectric constant, dielectric loss, dielectric loss tangent, and ac-conductivity measured w.r.t frequency and temperature. Fig. 5 (a), (b), and (c) represent the variation of the dielectric constant with frequency recorded at different temperatures for HEO samples synthesized at different synthesis parameters. It is

Table 1 — Different structural parameters evaluated through XRD pattern analysis

S. no	Parameters Sample	Lattice parameter (in Å)		Crystallite size (in nm)		Lattice strain $\times 10^{-3}$		Phase ratio Spinel/Rocksalt	Vol. phase fraction	
		Spinel	Rocksalt	Spinel	Rocksalt	Spinel	Rocksalt		Spinel	Rocksalt
1.	10BM-HEO20	8.408357	4.238836	101.80	57.075	1.2182	1.9351	1.38	0.58	0.42
2.	20BM-HEO20	8.394126	4.23141	72.39	58.62	1.5972	1.6297	1.17	0.54	0.46
3.	20BM-HEO10	8.395871	4.232244	56.503	55.421	1.9800	1.83065	1.07	0.51	0.49

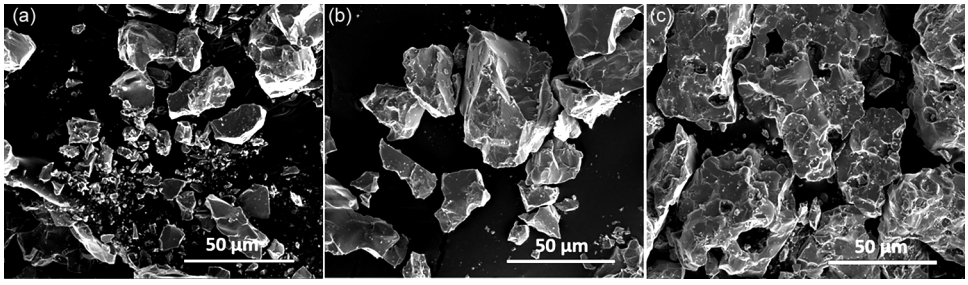

Fig. 3 — SEM micrographs of (a) 10BM-HEO-20, (b) 20BM-HEO-20, (c) 20BM-HEO-10 sintered at 1050 °C for different durations.

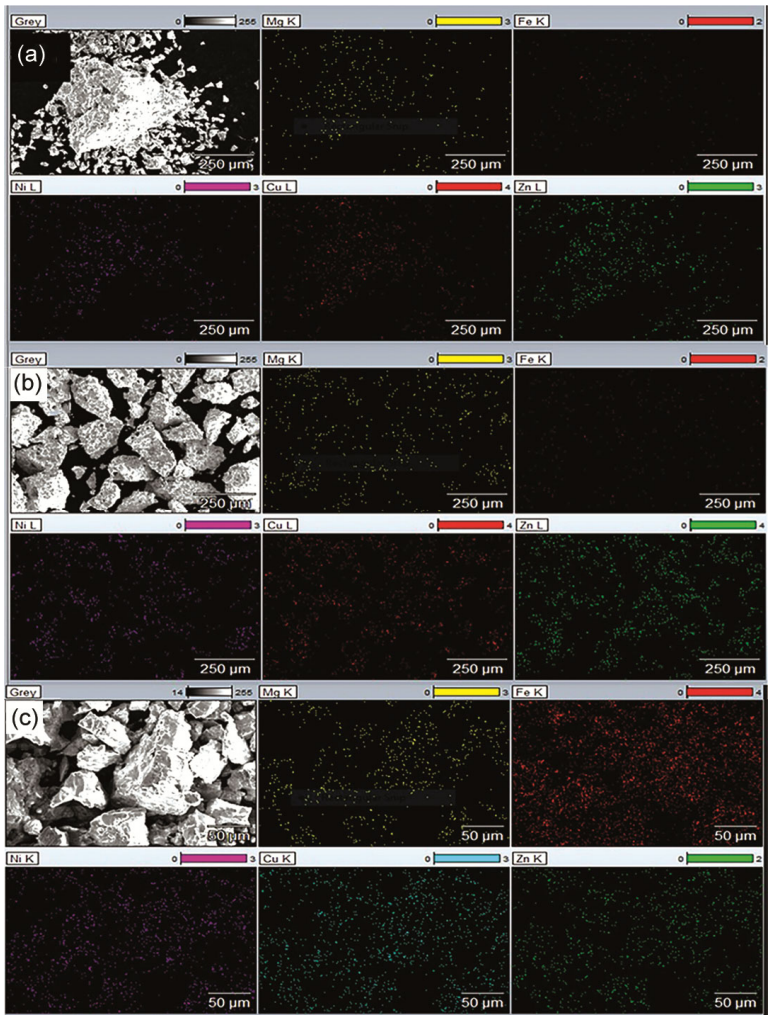

Fig. 4 — Elemental mapping of (a) 10BM-HEO-20, (b) 20BM-HEO-20, (c) 20BM-HEO-10 sintered at 1050 °C for different durations.

observed that for all the samples, the dielectric constant is high at the low-frequency range. This may be occurred due to the space charge polarisation at grain boundaries[47]. The value of ε' decreases as the frequency of the A.C. field increases.

Moreover, the dielectric constant becomes very low at the high frequency for each temperature, which clearly shows that the dielectric constant becomes independent of temperature at a higher frequency. The variation of the imaginary part of permittivity with frequency at different temperatures for the HEO sample synthesized at different parameters is shown in Fig. 5 (d,e,f). The value of dielectric loss is in decreasing trend for 10BM-HEO-20, 20BM-HEO-20 and 20BM-HEO-10 samples. The value of dielectric constant is different for the same HEO sample synthesized at different synthesized parameters (as shown in Fig. 5). This may occur due to the following reasons. (a) The variation in crystallite and/or particle size with a change in the processing parameters, (b)the change in the ratio of the formed spinel and rock-salt phase present in the selected HEO, and (c) the variation of lattice distortion with the variation of synthesis parameters. For conventional ceramic materials, it is well known that the $\varepsilon'$is directly proportional to particle size. The particle size creates two significant effects in regard to the dielectric response of the materials[48]. Firstly, the grain boundary has low permittivity; hence, the polarization at the grain boundary is either poor or negligible. Secondly, the depletion layer can form on the surface of the grain boundary, which creates discontinuity of the polarization on the grain surface, and hence polarization decreases as can be seen from Fig. 5. The dielectric constant decreases for samples10BM-HEO-20, 20BM-HEO-20, 20BM-HEO-10. The decrement in the dielectric constant value is directly related to a decrease in crystallite

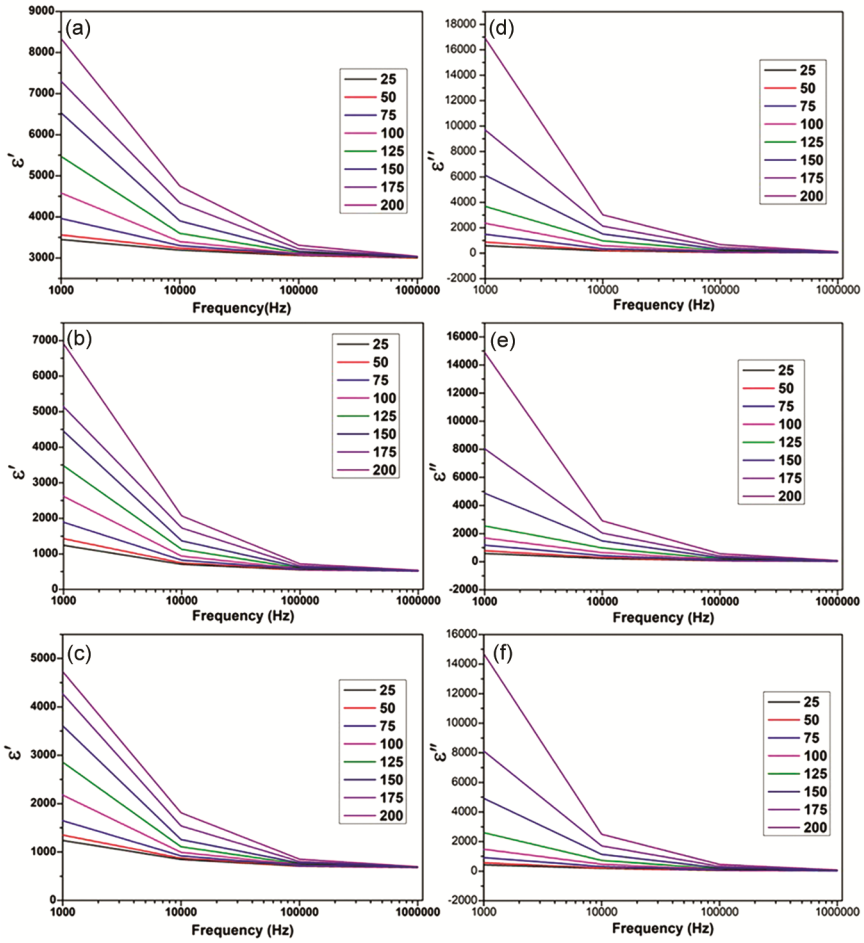

Fig. 5 — (a), (b), (c) represents the variation of $\varepsilon'$with frequency and (d), (e), (f) represents the variation of ε'' with frequency for 10BM-HEO-20, 20BM-HEO-20, and 20BM-HEO-10 at sintered temperature 1050 °C, respectively.

size(as shown in Table 1). Moreover, as can be seen from the SEM micrograph, 20BM-HEO-10 samples have large number of pores/vacant grains in particles. These pores further create discontinuity in the polarization and are responsible for a large number of the depletion layer. Hence increase in the number of grain boundaries, and porous microstructure reduced the net polarization for the 20BM-HEO-10[49,50,51]. Secondly, as can be seen from detailed XRD analysis, the phase fraction of the rock-salt structure increased, and the spinel phase was decreased in the following order for the samples 10BM-HEO-20, 20BM-HEO-20, and 20BM-HEO-10.It is well known that the spinel structure is more asymmetrical than rock-salt[52]; hence, the 10BM-HEO-20 sample has a high-value dielectric constant compared to the other two samples. It is well known that HEOs have distorted lattices due to different-sized cations in a unit cell. We can quantify the lattice distortion of the spinel structure by comparing the ratio of the intensity of (220) and (311) XRD peaks of the spinel phase and comparing these values with the value for the standard cobalt-based ferrite. For cobalt-based ferrite, the intensity ratio of I(220) and I(311) peaks is 0.35. Hence we can quantify the distortion by determining the value of $(I_{(220)}/I_{(311)})/0.35$[53]. The found value of lattice distortion for 10BM-HEO-20, 20BM-HEO-10 , and 20BM-HEO-20are 17,13 and 9%, respectively. Thus, the 10BM-HEO-20 sample has a more distorted unit cell compared to the other two samples; hence, it possessed a high dielectric constant value. We can say that the 10BM-HEO-20 has high value of the dielectric constant among other two HEOs samples due to the synergetic effect of the particle size, microstructure, volume phase fraction of spinel phase and the presence of more distorted lattice of the spinel phase in a particular HEO.

The ratio of the imaginary part to the real part of permittivity represents the significant energy loss. Fig. 6 depicts the value of tan δ, *i.e.*, the ratio of

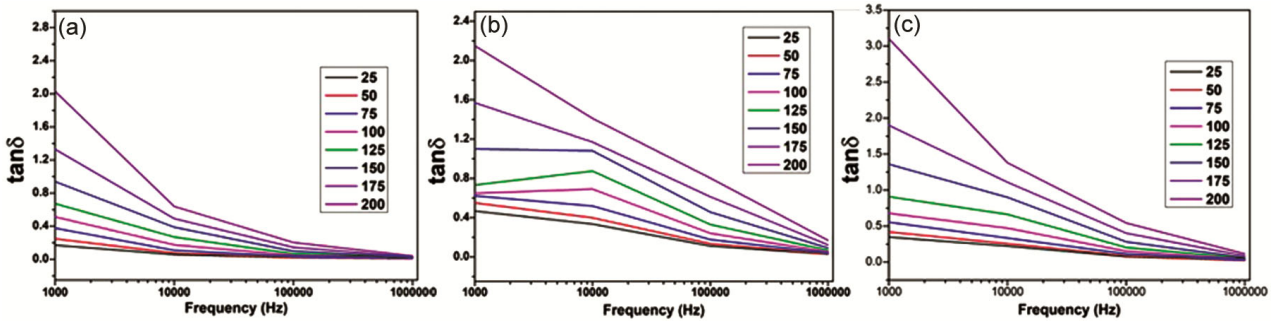

Fig. 6 — Variation of tan δ with frequency for (a) 10BM-HEO-20, (b) 20 BM-HEO-20, (c) 20BM-HEO-10 at sintered temperature 1050 °C.

imaginary to the real part of permittivity tan $\delta = \frac{\varepsilon''}{\varepsilon'}$. In general, such losses are mainly due to the migration of space charges. From the XRD analysis, it was concluded that the reduction in the crystallite size occurred for 20BM-HEO-20 and 20BM-HEO-10 as compared to 10BM-HEO-20, and the value of tan δ increases with the reduction in crystallite size of HEOs phases.

The A.C. conductivity is frequency dependent, and it is related to the dielectric constant (ε') *and* dielectric loss tangent(tanδ) through the relation:$\sigma_{ac}=\omega\varepsilon_0\varepsilon'\tan\delta$. σ_{ac} for the samples related to the hopping or tunneling of charge carrier in high-frequency region, where as in low-frequency region it is due to diffusion of carrier[54]. It is described by $\sigma_{ac} = A(2\pi f)^s + \sigma_{dc}$ where A is the characteristic parameter,f *is* frequency, and s is the exponent dependent on frequency and temperature. The plot between ln(σ_{ac}) and 1000/T for the frequency range of 10^3 Hz for the HEO samples synthesized at different synthesis parameters is shown in Fig. 7. The slope of the best-fitted straight line gives the activation energy. The activation energy (E_a) of the process correlated with σ_{ac} different samples is evaluated by Arrhenius law:$\sigma_{ac}=\sigma_o\, exp\left(\frac{-E_a}{k_BT}\right)$ where k_B is Boltzmann constant and σ_o is a pre-exponential factor. The value of activation energy for the 10BM-HEO-20, 20BM-HEO-20, and 20BM-HEO-10 at frequency 10^3 Hz are 0.211eV, 0.238eV, and 0.286eV, respectively. The slight increase in activation energy is due to a decrease in grain size and an increase in grain boundary in the samples. As a result, the transfer of electrons among grain decreases, and 10BM-HEO-20 behaves as more conducting than both samples. Moreover, for the 20BM-HEO-10 sample, the SEM image represents the formation of porous grain and minimizes the conductivity of the 20BM-HEO-10 sample.

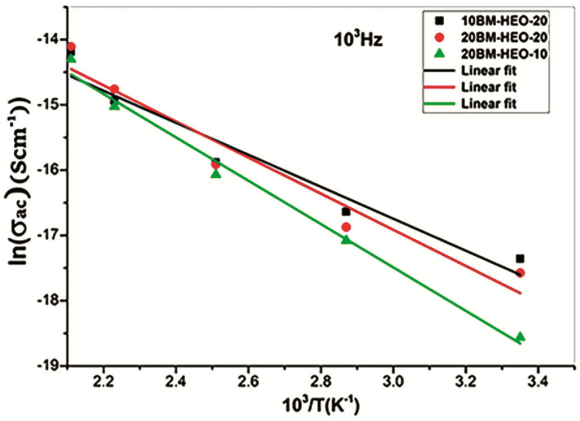

Fig. 7 — The plot between ln (σ_{ac}) Vs 10^3/T at frequency 10^3 Hz for (a) 10BM-HEO-20, (b) 20BM-HEO-20, (c) 20BM-HEO-10 at sintered temperature 1050 °C.

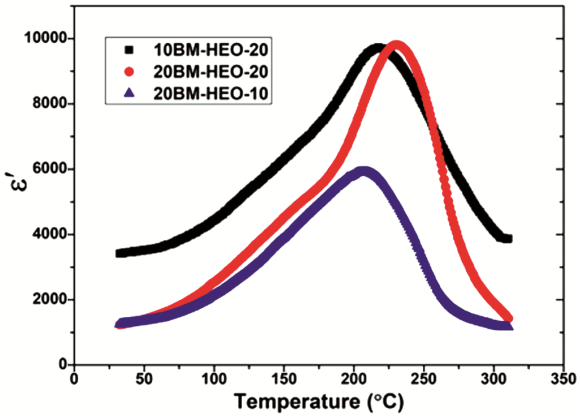

Fig. 8 — The plot of ε' Vs temperature at frequency 10^3 Hz for three samples.

To understand and investigate the ferroelectric to paraelectric transition for the selected HEO, we also performed the dielectric measurement at 10^3 Hz for the temperature range of room temperature to 310 °C. The change in dielectric constant as the function of temperature at frequency 10^3 Hz for three samples are shown in Fig 8. For all these samples, the value of dielectric constant increases with an increase in temperature due to expediting orientation of dipoles

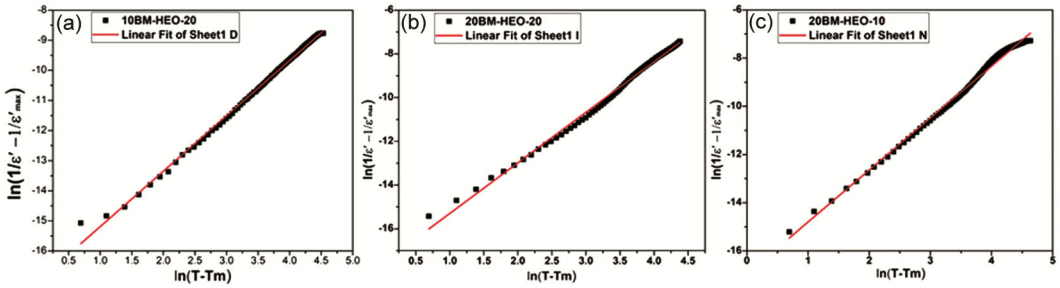

Fig. 9 — The plot of ln ($\frac{1}{\varepsilon'} - \frac{1}{\varepsilon'_{Max}}$) vs ln $(T - T_m)$ for sample (a) 10BM-HEO-20, (b) 20BM-HEO-20, (c) 20BM-HEO-10 at frequency 10^3 Hz.

and increase in phase stability as the removal of the sample's internal strain are associated with the crystal's synthesis process. It shows the maximum value at a transition temperature ($T_{C.}$), where there is phase transition occurs from ferroelectric (less symmetric) to paraelectric (more symmetric) phase. The dielectric constant of samples 10BM-HEO-20, 20BM-HEO-20, and 20BM-HEO-10 at transition temperature ($T_{C.}$) is 9731, 9813, and 5916, respectively. Curie -Weiss law describes the ferroelectric to para-electric phase transition as $\frac{1}{\varepsilon'} = \frac{T-T_C}{C}$, where C is curie-weiss constant and T_C is the curie temperature. To find the degree of disorder in the solid solution phase, the modified curie- Weiss law was developed by Uchino *et al.* and expressed as[55] $\frac{1}{\varepsilon'} - \frac{1}{\varepsilon'_{Max}} = \frac{(T-T_m)^Y}{c}$, where Y refers to the dielectric dispersion factor that shows the attribute of the phase transition, and Tm denotes the temperature at which ε'_{max} it achieves maximum value at a particular frequency[56]. Fig. 9(a-c) represents the plots of ln ($\frac{1}{\varepsilon'} - \frac{1}{\varepsilon'_{Max}}$) vs ln $((T - Tm)$ for three different samples at a frequency 10^3 Hz. The behaviour of phase transition for other frequency is almost same. The value of dispersion factor (Y) for10BM-HEO-20, 20BM-HEO-20 and 20BM-HEO-10 are 1.839,2.313, and 2.156, respectively. It is well known that for Y=1, the sample behaves as classical dielectric material, however the value of Y close to 2 represents the ideal relax or type ferroelectric material. From the depicted value of Y, we can conclude that all the three samples show diffuse transition and having Y value close to 2 hence these samples may behave as a good relax or ferroelectric material.

4 Conclusion

We successfully synthesized HEO phase with a modified solid state synthesis method, *i.e.*, ball-milling followed by sintering. The pre-ball milling before sintering is sufficient to produce the homogenous distribution of constituent oxide particles, which further enhances the diffusion of different oxides, and the formation of HEO phase was occurred for (Cu-Zn-Ni-Mg-Fe)O sample. The detailed XRD analysis confirmed the formation of spinel and rock-salt phase structure with different volume fractions for different synthesis parameters. The volume phase fraction for spinel and rock-salt phase for the selected (Cu-Zn-Ni-Mg-Fe)O oxide is found to be 58 and 42%, 54 and 46%, and 51 and 49% for 10BM-HEO-20, 20BM-HEO-20, 20BM-HEO-10 samples, respectively. The value of dielectric constant decreased for the sample 10BM-HEO-20, 20BM-HEO-20 and 20 BM-HEO-10 HEOs due to the synergistic effect of decrease in particle size, volume phase fraction of spinel phase as well as more distorted unit cells of spinel HEO phase. Moreover, the value of dielectric loss is in decreasing trend for 10BM-HEO-20, 20BM-HEO-20 and 20BM-HEO-10 samples.. We also evaluated the activation energy and found it to be 0.211eV, 0.238eV, and 0.286eV at a frequency 10^3 Hz for the 10BM-HEO-20, 20BM-HEO-20, and 20BM-HEO-10 samples, respectively the slight increase in activation energy is associated with an increase in grain boundary with the synthesis parameters. Also the dispersion factor for 10BM-HEO-20, 20BM-HEO-20, and 20BM-HEO-10 and found to be 1.839, 2.313, and 2.156, respectively. Thus in conclusion we can say that the dielectric properties of HEO can be tuned broadly by the variation of synthesized parameters.

Acknowledgment

The author would like to acknowledge the Department of Physics, Central University of South Bihar (CUSB), Gaya, Bihar, for the instrumentation facilities. The authors also acknowledge the financial

support from UGC-DAE CSR through a Collaborative Research Scheme (CRS) project number CRS/2021-22/01/381.

References:

1 Cantor B, Chang I T H, Knight P & Vincent A J B, *Mater Sci Eng* A, 375–377 (2004) 213.
2 Yeh J W, Chen S K, Lin S J, Gan J Y, Chin T S, Shun T T, Tsau C H & Chang S Y, *Adv Eng Mater,* 6 (2004) 299.
3 Tsai M H & Yeh J W, *Mater Res Lett,* 2 (2014) 107.
4 Rost C M, Sachet E, Borman T, Moballegh A, Dickey E C, Hou D Jones J L, Curtarolo S & Maria J P, *Nat Commun,* 6 (2015) 8485.
5 Gild J, Zhang Y, Harrington T, Jiang S, Hu T, Quinn M C, Mellor W M, Zhou N, Vecchio K & Luo J, *Sci Rep,* 6 (2016) 37946.
6 Zhang R Z, Gucci F, Zhu H, Chen K & Reece M J, *Inorg Chem,* 57 (2018) 13027.
7 Glasscott M W, Pendergast A D, Goines S, Bishop A R, Hoang A T, Renault C & Dick J E, *Nat Commun,* 10 (2019) 2650.
8 Jin T, Sang X, Unocic R R, Kinch R T, Liu X, Hu J, Liu H & Dai S, *Adv Mater,* 30 (2018) 1707512.
9 Sarker P, Harrington T, Toher C, Oses C, Samiee M, Maria J P, Brenner D W, Vecchio K S & Curtarolo S, *Nat Commun,* 9 (2018) 4980.
10 Sarkar A, Breitung B & Hahn H, *Scr Mater,*187 (2020) 43.
11 Hong W, Chen F, Shen Q, Han Y, Fahrenholtz W G & Zhang L, *J Am Ceram Soc,*102 (2019) 2228.
12 Dabrowa J, Stygar M, Mikuła A, Knapik A, Mroczka K, Tejchman W, Danielewski M & Martin M, *Mater Lett,* 216 (2018) 32.
13 Sarkar A, Velasco L, Wang D, Wang Q, Talasila G, Biasi L D, Kübel C, Brezesinski T, Bhattacharya S S, Hahn H & Breitung B, *Nat Commun,* 9 (2018) 3400.
14 Chellali M R, Sarkar A, Nandam S H, Bhattacharya S S, Breitung B, Hahn H & Velasco L, *Scr Mater,* 166 (2019) 58.
15 Bérardan D, Franger S, Dragoe D, Meena A K & Dragoe N, *Pss Rrl,* 10 (2016) 328.
16 Gild J, Samiee M, Braun J L, Harrington T, Vega H, Hopkins P E, Vecchio K & Luo J, *J Eur Ceram,* 38 (2017) 3578.
17 Djenadic R, Sarkar A, Clemens O, Loho C, Botros M, Chakravadhanula V S K, KübelC, Bhattacharya S S, Gandhi A S & Hahn H, *Mater Res Lett,* 5 (2017) 102.
18 Sarkar A, Loho C, Velasco L, Thomas T, Bhattacharya S S, Hahn H & Djenadic R, *Dalton Trans,* 46 (2017) 12167.
19 Tseng K, Yang Q, McCormack S J & Kriven W M, *J Am Ceram Soc,* 103 (2020) 569.
20 Teng Z, Zhu L, Tan Y, Zeng S, Xia Y, Wang Y & Zhang H, *J Eur Ceram,* 40 (2020) 1639.
21 Vinnik D A, Trofimov E A, Zhivulin V E, Zaitseva O V, Gudkova S A, Starikov A Y, Zherebtso D A, Krisanova A A, Habner M & Niewa R, *Ceram Int,* 45 (2019) 12942.
22 Zhao C, Ding F, Lu Y, Chen L & Hu Y, *Angew Chem Int Ed,* 59 (2020) 264.
23 Parida T, Karati A, Guruvidyathri K, Murty B S & Markandeyulu G, *Scr Mater,* 178 (2020) 513.
24 Gupta A K, Kumari P, Prakash A, Giri N K & Shahi R R, Ceram Int, 48 (2022) 36258.
25 Musico B, Wright Q, Ward T Z, Grutter A, Arenholz E, Gilbert D, Mandrus D & Keppens V, *Phys Rev Mater,* 3 (2019) 104416.
26 Kumari P, Gupta A K, Mishra R K, Ahmad S & Shahi R R, *J Magn Magn Mater,* 554 (2022) 169142.
27 Chen H, Qiu N, Wu B, Yang Z, Sun S & Wang Y, *RSC Adv,* 10 (2020) 9736.
28 Mao A, Xiang H Z, Zhang Z G, Kuramoto K, Yu H & Ran S, *J Magn Magn Mater,* 484 (2019) 245.
29 Talluri B, Aparna M L, Sreenivasulu N, Bhattacharya S S & Thomas T, *J Energy Storage,* 42 (2021) 103004.
30 Pu Y, Zhang Q, Li R, Chen M, Du X & Zhou S, *Appl Phys Lett,* 115 (2019) 223901.
31 Gupta A K, Prakash A & Shahi R R, High Entropy Materials: An Emerging Material for Battery and Supercapacitive Applications'in Materials Science: Future Aspects: Edtd by Awasthi K, Srivastava A & Tripathi M, Nova publication, (2022) 77.
32 Abdelhafiz A, Wang B, Harutyunyan A R & Li Z, *Adv Energy Mater,* 12 (2022) 2200742.
33 Zhao S, Lin J, Wu P, Ye C, Li Y, Li A, Jin X, Zhao Y, Chen G, Qiu Y & Ye D, *ACS Appl Mater Interfaces,* 13 (2021) 48764.
34 Braun J L, Rost C M, Lim M, Giri A, Olson D H, Kotsonis G N, Stan G, Brenner D W, Maria J P & Hopkins P E, *Adv Mater,* 30 (2018) 1805004.
35 Cheng B, Lou H, Sarkar A, Zeng Z, Zhang F, Chen X, Tan L, Prakapenka V, Greenberg E, Wen J, Djenadic R, Hahn H & Zeng Q, *Commun Chem,* 2 (2019) 114.
36 Lun Z, Ouyang B, Kwon D H, Ha Y, Foley E E, Huang T Y, Cai Z, Kim H, Balasubramanian M, Sun Y, Huang J, Tian Y, Kim H, McCloskey B D, Yang W, Clément R J, Ji H & Ceder G, *Nat Mater,* 20 (2020) 214.
37 Wang Q, Sarkar A, Wang D, Velasco L, Azmi R, Bhattacharya S S, Bergfeldt T, Du¨vel A, Heitjans P, Brezesinski T, Hahn H & Breitung B, *Energy Environ Sci,* 12 (2019) 2433.
38 Liang B, Ai Y, Wang Y, Liu C, Ouyang S & Liu M, *Mater,13* (2020) 5798.
39 Lou Z, Xu X, Zhang P, Gong L, Chen Q, Xu J, Rydosz A & Gao F, *J Mater Res Technol,* 21 (2022) 850.
40 Bérardan D, Franger S, Meena A K & Dragoe N, *J Mater Chem A,* 4 (2016) 9536.
41 Chen K, Pei X, Tang L, Cheng H, Li Z, Li C & Zhang X, *J Eur Ceram Soc,* 38 (2018) 4161.
42 Radoń A, Hawełek L, Łukowiec D, Kubacki J & Włodarczyk P, *Sci Rep,* 9 (2019) 20078.
43 Zhou S, Pu Y, Zhang Q, Shi R, Guo X, Wang, W Ji J, Wei T & Ouyang T, *Ceram Int,* 46 (2020) 7430.
44 Vinnik D A, Trofimov E A, ZhivulinV E, Gudkova S A, Zaitseva O V, Zherebtsov D A, Starikov A Y, Sherstyuk D P, Amirov A A, Kalgin A V, Trukhanov S V & Podgornov F V, *Nanomater,* 10 (2020)..
45 Stygara M, Dąbrowaa J, Moździerza M, Zajusza M, Skubidab W, Mroczkac K, Berentd K, Świerczekb K, Danielewskia M, *J Eur Ceram Soc*, 40 (2020) 1644.
46 Mishra R K & Shahi R R, *J Magn Magn Mater,* 48 (2019) 83.
47 Rayssi C H, Kossi S E, Dhahri J & Khirouni K, ***RSC Adv,* 8 (**2018) 17139.
48 Lee H G & Kim H G, *J Appl Phys,* 67 (1990) 2024.

49 Curecheriu L, Balmus S B, Buscaglia M T, Buscaglia V, Ianculescu A & Mitoseriu L, *J Am Ceram Soc,* 95 (2012) 3912.
50 Perm S J, Alford N MCN, Templeton A, Wang X, Xu M, Reece M & Schrapelt K, *J Am Ceram Soc,* 80 (1997) 1885.
51 Mudinepalli V R, Feng L, Lin W C & Murty B S, *J Adv Ceram,* 4 (2015) 46.
52 Dunitz J D & Orgel L, *J Phys Chem Solids,* 3 (1957) 20.
53 Mao A, Quan F, Xiang H Z, Zhang Z G & Xia A I, *J Mol Struct,* 1194 (2019) 11.
54 Rayssi CH, Rhouma F I H, Jemai D & Khirouni K, *Appl Phys A,* 123 (2017) 778.
55 Uchino K & Relaxor, *Ferroelectr,* **151** (1994) 321.
56 Uchino K & Nomura S, *Ferroelectr,* 44 (1982) 55.